Supplementary Information

Topological phase singularities in atomically thin high-refractive-index materials

Georgy Ermolaev,[1] Kirill Voronin*,[1, 2] Denis G. Baranov,[1] Vasyl Kravets,[3] Gleb Tselikov,[1] Yury Stebunov,[4] Dmitry Yakubovsky,[1] Sergey Novikov,[1] Andrey Vyshnevyy,[1] Arslan Mazitov,[1, 5] Ivan Kruglov,[1, 5] Sergey Zhukov,[1] Roman Romanov,[6] Andrey M. Markeev,[1] Aleksey Arsenin,[1] Kostya S. Novoselov,[4, 7, 8] Alexander Grigorenko,[3] and Valentyn Volkov[1]*

[1]Center for Photonics and 2D Materials, Moscow Institute of Physics and Technology, Dolgoprudny 141700, Russia.

[2]Skolkovo Institute of Science and Technology, Moscow 121205, Russia.

[3]Department of Physics and Astronomy, University of Manchester, Manchester M13 9PL, UK.

[4]National Graphene Institute (NGI), University of Manchester, Manchester M13 9PL, UK.

[5]Dukhov Research Institute of Automatics (VNIIA), Moscow 127055, Russia.

[6]National Research Nuclear University MEPhI (Moscow Engineering Physics Institute), Moscow 115409, Russian Federation.

[7]Department of Materials Science and Engineering, National University of Singapore, Singapore 03-09 EA, Singapore.

[8]Chongqing 2D Materials Institute, Chongqing 400714, China.

e-mail: volkov.vs@mipt.ru

Table of Contents

Supplementary Note 1: Derivation of the conditions for the observation of the zero-reflection points

In this work, ultrathin (with a thickness of about 5 nm or less) films of materials with a high refractive index are considered. In this case, we can assume that the wave phase acquired during the path through the film is small: $nk_0t \ll 1$, where $k_0 = \frac{\omega}{c}$, ω is the wave frequency, c is the speed of light, t is the thickness of the film and n is the refractive index of the film material. This allows us in all analytical calculations to replace the film with a two-dimensional (2D) conductive layer. The effective 2D conductivity, σ is related to the dielectric permittivity, ε, as: $\sigma = \frac{\varepsilon ct}{2i\lambda_0}$, where λ_0 is the free-space wavelength. We also use the normalized conductivity $\alpha = 2\pi\sigma/c = \frac{\varepsilon k_0 t}{2i}$, introduced for convenience. Due to this approximation, it is possible to obtain a relatively simple explicit expression for the dielectric constant that provides zero reflection at a given angle of incidence and wavelength of the incident light.

For this, we solve the standard linear system of equation for the reflection of the electromagnetic wave in the three-layer medium (see Figure 1a) but with the modified boundary condition for the magnetic field on the interface with 2D conductivity:

$$\boldsymbol{e}_z \times (\boldsymbol{H}_{t1} - \boldsymbol{H}_{t2}) = 2\alpha \boldsymbol{E}_t \tag{1}$$

where the subscript "t" in Eq. (1) means the in-plane components. Solving the linear system, we obtain

$$r_s = \frac{(q_{1z} - 2\alpha)(q_{2z}\cos k_{2z}\,d - iq_{3z}\sin k_{2z}\,d) - q_{2z}(q_{3z}\cos k_{2z}\,d - iq_{2z}\sin k_{2z}\,d)}{(q_{1z} + 2\alpha)(q_{2z}\cos k_{2z}\,d - iq_{3z}\sin k_{2z}\,d) + q_{2z}(q_{3z}\cos k_{2z}\,d - iq_{2z}\sin k_{2z}\,d)} \tag{2}$$

Applying the condition $r_s = 0$, we find α and dielectric permittivity of the film

$$\varepsilon_s = \frac{1}{k_0 t}\left(iq_{1z} + q_{2z}\frac{q_{3z} - iq_{2z}\tan(k_{2z}d)}{q_{3z}\tan(k_{2z}d) + iq_{2z}}\right) \tag{3}$$

Analogously, for the p-polarized light we obtain

$$\varepsilon_p = \frac{1}{k_0 t}\left(\frac{i\varepsilon_1}{q_{1z}} + \frac{\varepsilon_2}{q_{2z}}\frac{\frac{\varepsilon_3}{q_{3z}} - \frac{i\varepsilon_2}{q_{2z}}\tan(k_{2z}d)}{q_{3z}\tan(k_{2z}d) + \frac{i\varepsilon_2}{q_{2z}}}\right) \quad (4)$$

Supplementary Note 2: Phase singularities in high-refractive-index materials

The effect of phase singularity is general and applicable not only to layered structures considered in the main part of the manuscript, but to a broader family of materials, for example, quasi-2D metals as well. Therefore, it allows to adjust the positions of topological points through the change of high-refractive-index materials. This concept is illustrated in Supplementary Figure 1 where topological points for different materials are collected.

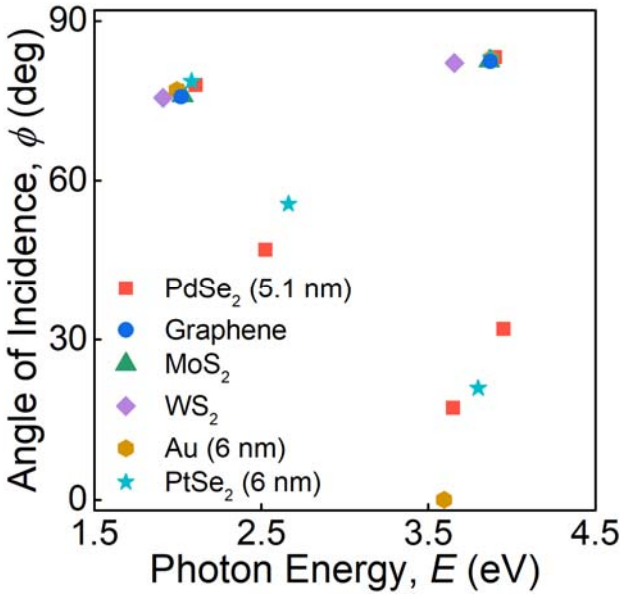

Supplementary Figure 1. Abundance of phase singularities in high-refractive-index materials. Calculated topological points using Supplementary Equation (4) for high-refractive-index materials. Optical constants for calculation were adopted from several reports. Optical constants for calculation were adopted from several reports.[1–5]

Supplementary Note 3: Optical anisotropy in $PdSe_2$

$PdSe_2$ is a naturally anisotropic material with a unique puckered pentagonal lattice structure (Figure 3a) with a point group D_{2h} and a space group *Pbca*. To get the qualitative insight into optical anisotropy, we theoretically calculated the real and imaginary parts of dielectric tensor of $PdSe_2$ within the single-shot GW approach[6] implemented in ViennaAb Initio Simulation Package (VASP).[7,8] Core electrons and their effect on valence electrons were described in generalized gradient approximation (Perdew-Burke-Ernzerhof functional)[9,10] using GW pseudopotentials with 18 and 24 valence electrons for Pd and Se respectively. Cutoff energy for plane waves basis set was 450 eV, and the first Brillouin zone was sampled with Γ-centered 4×4×3 mesh. The resulted optical constants are plotted in Supplementary Figure 2.

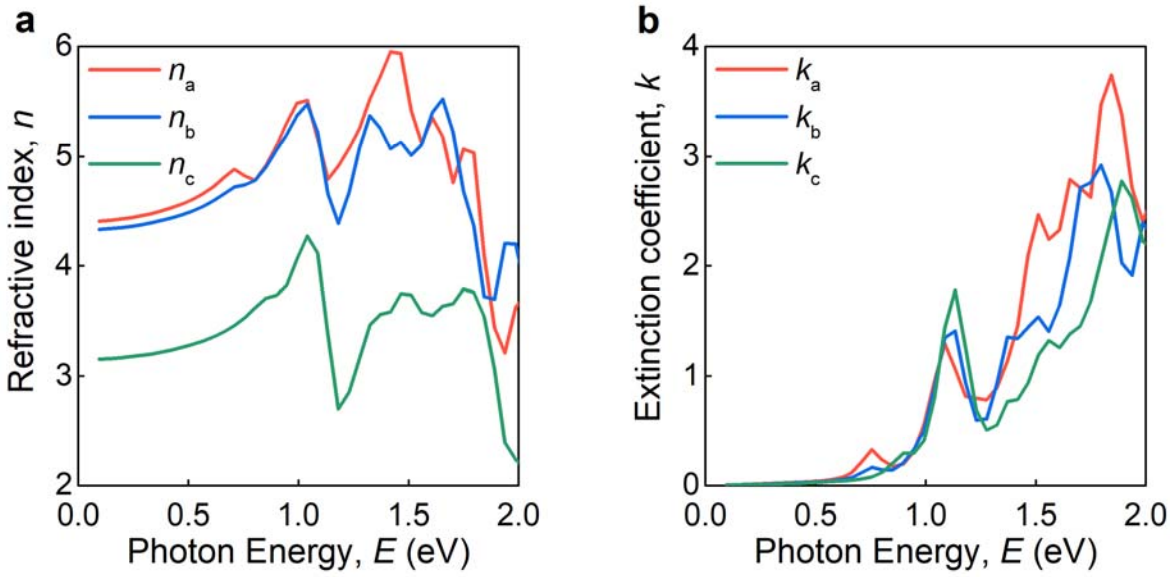

Supplementary Figure 2. Theoretical optical anisotropy in $PdSe_2$. a Anisotropic refractive indices and **b** extinction coefficients along crystallographic axes *a*, *b*, and *c*.

To experimentally reveal $PdSe_2$ optical anisotropy, we measured Mueller Matrix via imaging ellipsometer Accurion nanofilm_ep4. Mueller Matrix ***M*** relates the incident light polarization

expressed in terms of Stokes parameters $S^{inc} = (S_1^{inc}, S_2^{inc}, S_3^{inc}, S_4^{inc})$ to the polarization of the light reflected from the sample $S^{ref} = (S_1^{ref}, S_2^{ref}, S_3^{ref}, S_4^{ref})$:[11]

$$S^{ref} = \boldsymbol{M} S^{inc} \tag{5}$$

or in a detailed form:

$$\begin{cases} S_1^{ref} = m_{11}S_1^{inc} + m_{12}S_2^{inc} + m_{13}S_3^{inc} + m_{14}S_4^{inc} \\ S_2^{ref} = m_{21}S_1^{inc} + m_{22}S_2^{inc} + m_{23}S_3^{inc} + m_{24}S_4^{inc} \\ S_3^{ref} = m_{31}S_1^{inc} + m_{32}S_2^{inc} + m_{33}S_3^{inc} + m_{34}S_4^{inc} \\ S_4^{ref} = m_{41}S_1^{inc} + m_{42}S_2^{inc} + m_{43}S_3^{inc} + m_{44}S_4^{inc} \end{cases} \tag{6}$$

where m_{ij} are normalized to m_{11}, which is set to unity. In turn, Stokes parameters are observable quantities with the following definitions: the first Stokes parameter S_1 is the total intensity of light; S_2 characterizes linear horizontal (vertical) polarization; the parameter S_3 characterizes linear +45° polarization, and the parameter S_4 characterizes right and left circular polarization of the beam.[11] Therefore, Stokes parameters describe light, while Mueller Matrix describes the sample of interest. More interestingly, off-diagonal elements of Mueller Matrix (m_{13}, m_{14}, m_{23}, m_{24}, m_{31}, m_{32}, m_{41}, m_{42}) indicate whether the sample has in-plane optical anisotropy (some off-diagonal elements are nonzero) or behaves isotropically (all off-diagonal elements are zero).[11]

In our device, we have access to 11 elements of Mueller Matrices shown in Supplementary Figure 3. Clearly, non-diagonal elements are non-zero, thus confirming in-plane optical anisotropy of $PdSe_2$. Nevertheless, Mueller Matrices values differ from point to point. This difference originates, tentatively, from the random film growth during the CVD process. This assumption is in line with the value's distribution following the Gaussian law (Supplementary Figure 4), showing that in-plane optical axis of $PdSe_2$ orients randomly. More importantly, the average of off-diagonal elements of Mueller Matrices is zero which proves isotropic optical response of the $PdSe_2$ sample at large scale.

Similar situation is also observed in optical microscope. During the rotation of polarizer, sample's parts interchange colors as shown in Supplementary Figure 5 thereby validating local anisotropic response. Additionally, the Raman spectroscopy also demonstrates that the intensity of phonon modes differs for various polarizations of the excitation beam and again depends on position of the sample. Nevertheless, point measurements reveal expected dependence of the intensity $I(A_g^1)$ on angle α between the optical axis and the excitation beam polarization (Supplementary Figure 6):[12]

$$I(A_g^1) = (I_a \cos^2(\alpha) + I_b \sin^2(\alpha))^2 \quad (7)$$

where I_a and I_b are eigenvalues of Raman tensor for A_g^1 phonon mode along crystallographic *a* and *b*-axes. These observations (ellipsometric, optical, and Raman) allow us to treat $PdSe_2$ as an isotropic sample in the main part of the paper.

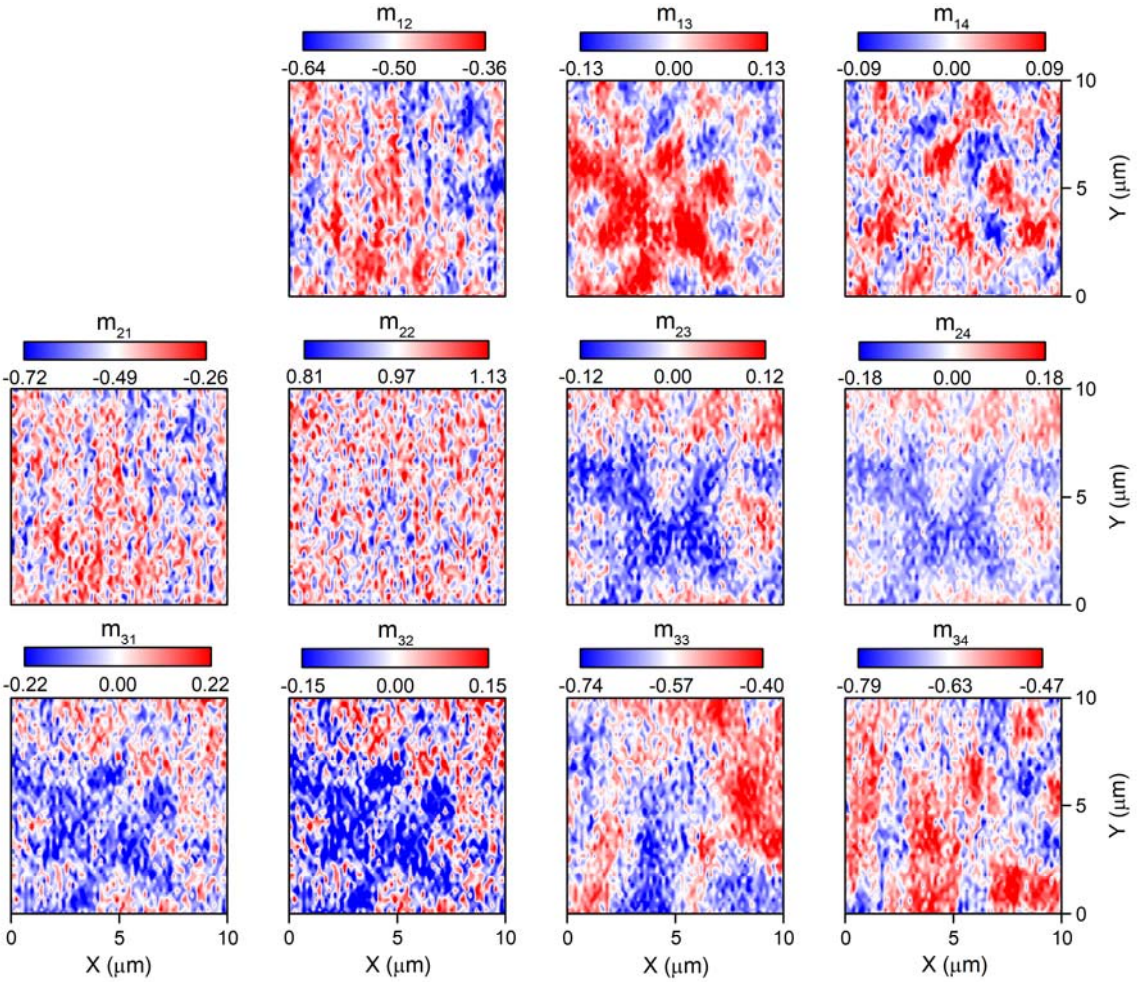

Supplementary Figure 3. Anisotropy in $PdSe_2$ imaged through Mueller Matrix. Mueller Matrix recorded at 50° and $\lambda = 430$ nm. Nonzero non-diagonal blocks of Mueller Matrix (m_{13}, m_{14}, m_{23}, m_{24}, m_{31}, m_{32}) shows that $PdSe_2$ has in-plane anisotropy distributed randomly.

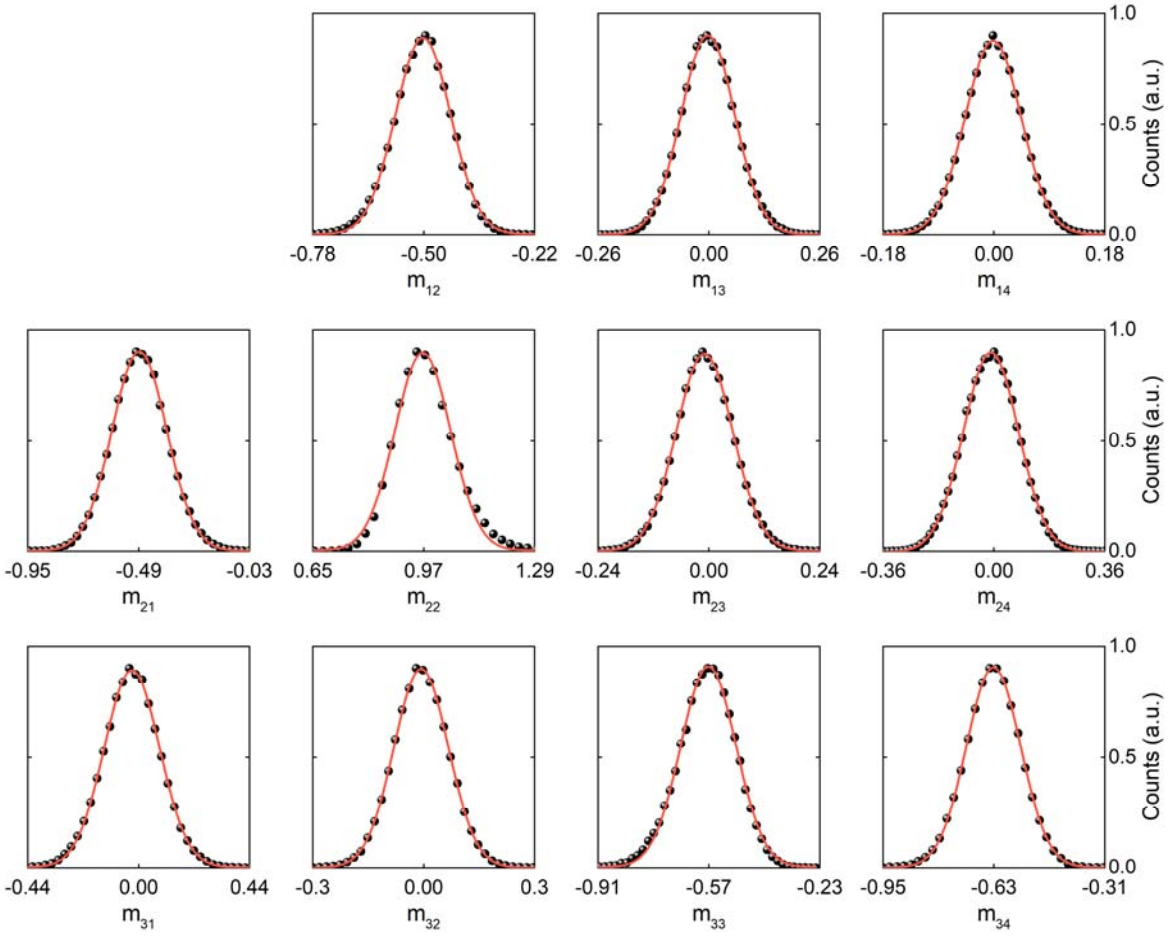

Supplementary Figure 4. Distribution of Mueller Matrix values. Relative frequency of Mueller Matrix values from Supplementary Figure 3 follows Gaussian distribution (red line) with zero average for non-diagonal blocks (m_{13}, m_{14}, m_{23}, m_{24}, m_{31}, m_{32}), thus validating isotropic response of $PdSe_2$ at a macroscale.

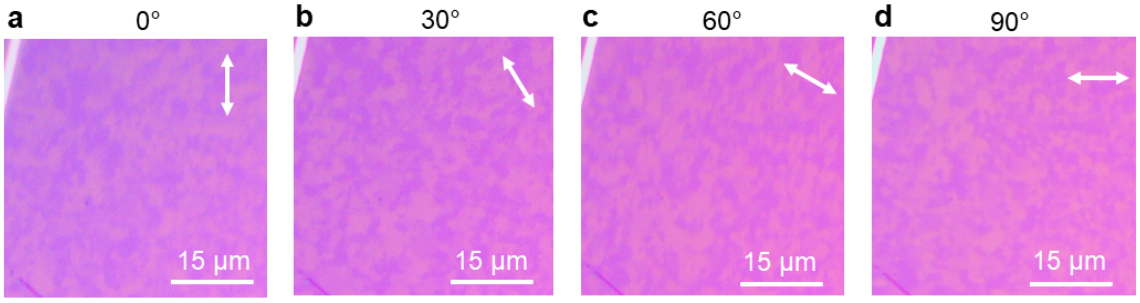

Supplementary Figure 5. Optical images of $PdSe_2$ at polarized illumination. Macroscopic view of $PdSe_2$ with polarizer at **a** 0°, **b** 30°, **c** 60°, and **d** 90°.

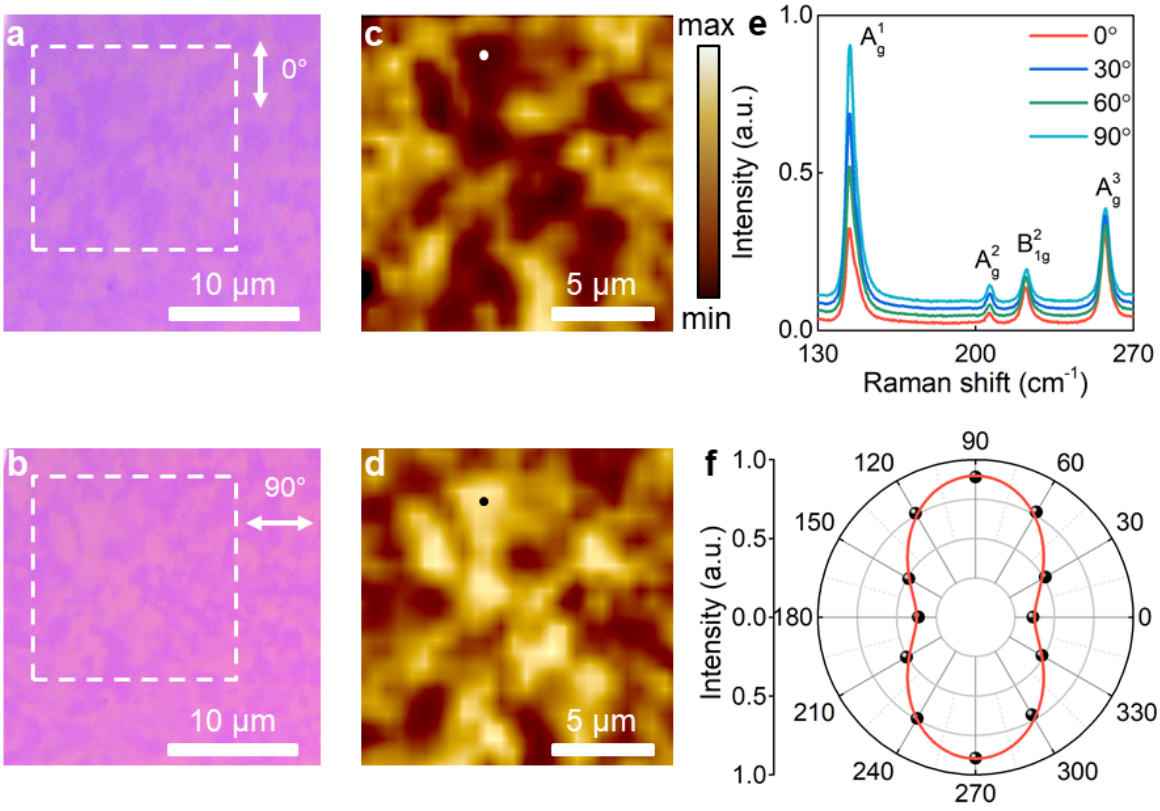

Supplementary Figure 6. Polarized Raman spectroscopy of $PdSe_2$. a-b Optical images at Raman microscope at perpendicular orientations of polarizer. **c-d** Raman maps for intensity of A_g^1 taken at perpendicular polarizer angles from the sample area labeled by the dashed square in **(a-b)** panel, respectively. **e** Raman spectra for 4 polarizer angles taken at point denoted by white and black points in **(c-d)** panels. **f** The dependence of A_g^1 intensity on the angle of polarizer. The red line is a theoretical curve defined through Supplementary Equation (7).

Supplementary Note 4: Determination of optical constants of $PdSe_2$ from reflection and ellipsometry measurements

To experimentally retrieve isotropic dielectric response of $PdSe_2$ ε_{PdSe_2}, we fitted ellipsometric spectra of Ψ and Δ at 6 incidence angles, (45, 50, 55, 60, 65, 70°) and reflection spectrum at normal incidence presented in Supplementary Figure 7 a-b and c, respectively. We used 5 Tauc-Lorentz oscillators $\varepsilon'_{TL} + i\varepsilon''_{TL}$ model to describe excitonic response[4] of $PdSe_2$ and Drude oscillator ε_{Drude} to

account metallic response from inherent doping revealed by XPS of valence band shown in Supplementary Figure 7d:

$$\varepsilon_{\mathrm{PdSe_2}} = \varepsilon_\infty + \varepsilon_{\mathrm{Drude}} + \sum_{j=1}^{5}\left(\varepsilon'_{\mathrm{TL},j} + i\varepsilon''_{\mathrm{TL},j}\right) =$$

$$= \varepsilon_\infty + \frac{-\hbar^2}{\varepsilon_0\rho(\tau E^2 + i\hbar E)} + \sum_{j=1}^{5}\left(\frac{2}{\pi}\mathrm{v.p.}\int_{E_g}^{\infty}\frac{\xi\varepsilon''_{TL,j}(\xi)}{\xi^2 - E^2}d\xi + iH_{E_g}(E)\frac{1}{E}\frac{A_j E_{0,j} C_j\left(E - E_g\right)^2}{\left(E^2 - E_{0,j}^2\right)^2 + C_j^2 E^2}\right) (8)$$

where ε_∞ is a contribution in the dielectric function of high energy interband transition, E is photon energy, $\hbar$ is Planck's constant, ε_0 is vacuum permittivity, ρ is resistivity, τ is mean scattering time, E_g is optical band gap, $H_{E_g,}(E)$ is Heaviside step function equal one if $E > E_{g,j}$ and zero otherwise, A_j, C_j, and $E_{0,j}$ are strength, broadening term, and peak central energy of j^{th} Tauc-Lorentz oscillator, respectively. Final parameters for $PdSe_2$ optical model are $\varepsilon_\infty = 2.20 \pm 0.02$, $\rho = (0.0115 \pm 0.0007)$ Ohm·cm, $\tau = (1.34 \pm 0.07)$ fs, $E_g = (0.879 \pm 0.004)$ eV with Tauc-Lorentz oscillator parameters collected in Supplementary Table 1.

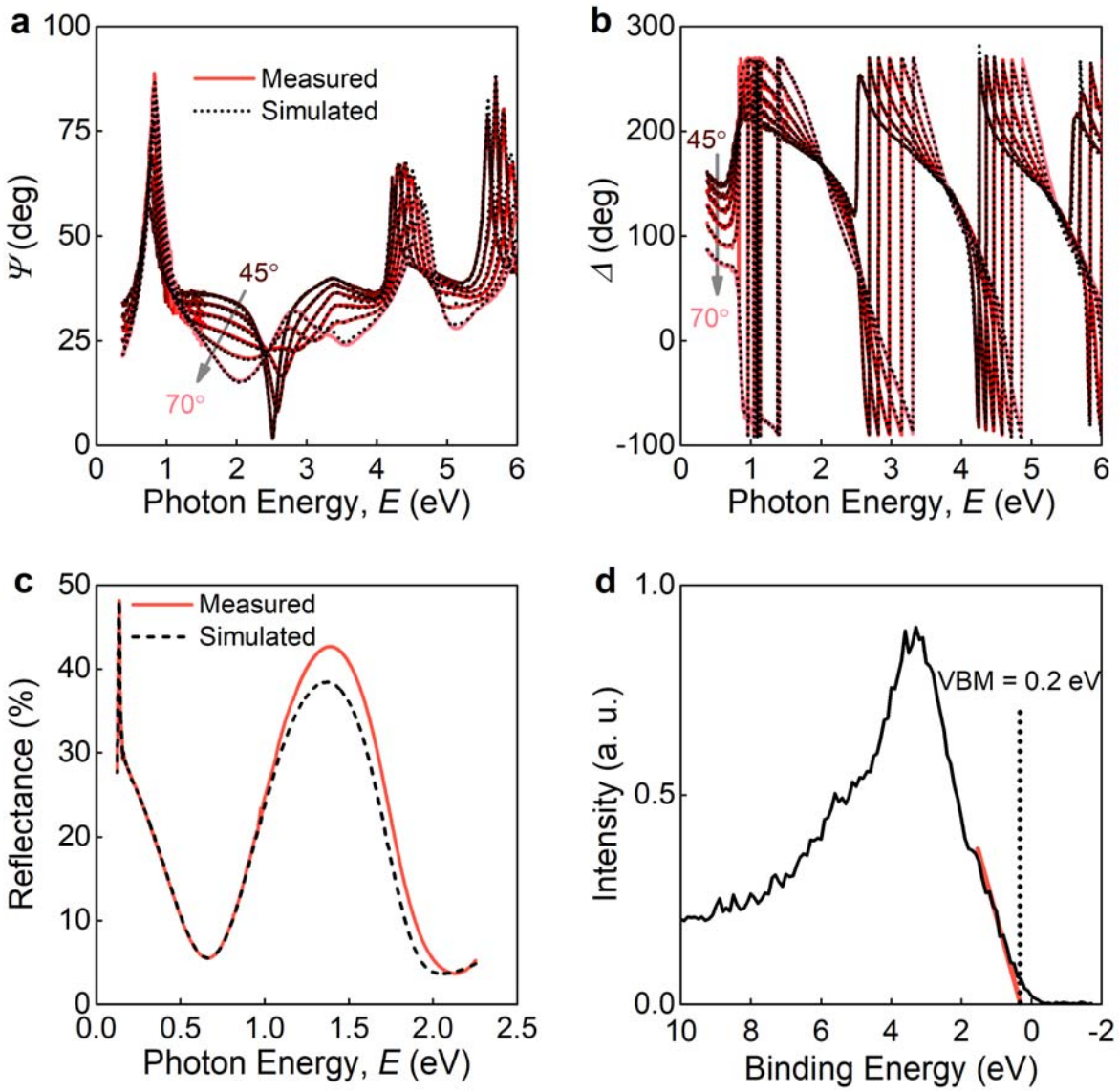

142

143 **Supplementary Figure 7. Determination of $PdSe_2$ optical constants. a-b** Experimentally
144 measured and simulated (based on optical model defined via Supplementary Equation (8))
145 ellipsometric parameters Ψ (amplitude) and Δ (phase), and **c** normal incidence reflectance spectra
146 for $PdSe_2$(5.1 nm)/SiO_2(280 nm)/Si. **d** Valence band revealed by XPS shows that maximum (VBM)
147 is shifted from the Fermi level by 0.2 eV. It corresponds to p-type conductivity since $PdSe_2$
148 bandgap is about 0.8 eV and undoped sample should have about 0.4 eV difference between Fermi
149 level and VBM.[13]

Supplementary Table 1. Parameters of Tauc-Lorentz oscillators describing $PdSe_2$ excitonic response.

Tauc-Lorentz oscillator	A eV	E_0 eV	C eV
#1	54.8 ± 0.6	2.027 ± 0.002	1.172 ± 0.005
#2	4.72 ± 0.15	3.090 ± 0.005	0.789 ± 0.015
#3	6.4 ± 0.2	3.766 ± 0.005	0.958 ± 0.017
#4	0.377 ± 0.012	5.048 ± 0.005	0.163 ± 0.014
#5	35 ± 1	6.89 ± 0.04	9.54 ± 0.29

Supplementary Note 5: Ellipsometry measurement of $PdSe_2$ in water medium

For $PdSe_2/SiO_2/Si$ to be a reliable sensor, $PdSe_2$ should preserve its properties (in particular, optical constants from Figure 3k) when contacted with water solution. To confirm $PdSe_2$ water stability, we measured ellipsometric maps in the vicinity of topological zero of the system. Evidently, measured and simulated (based on dielectric function from Figure 3k) spectra in Supplementary Figure 8 are in close agreement thereby validating that water has no effect on $PdSe_2$ dielectric function. Hence, we can safely use $PdSe_2$ as a liquid refractive index sensor.

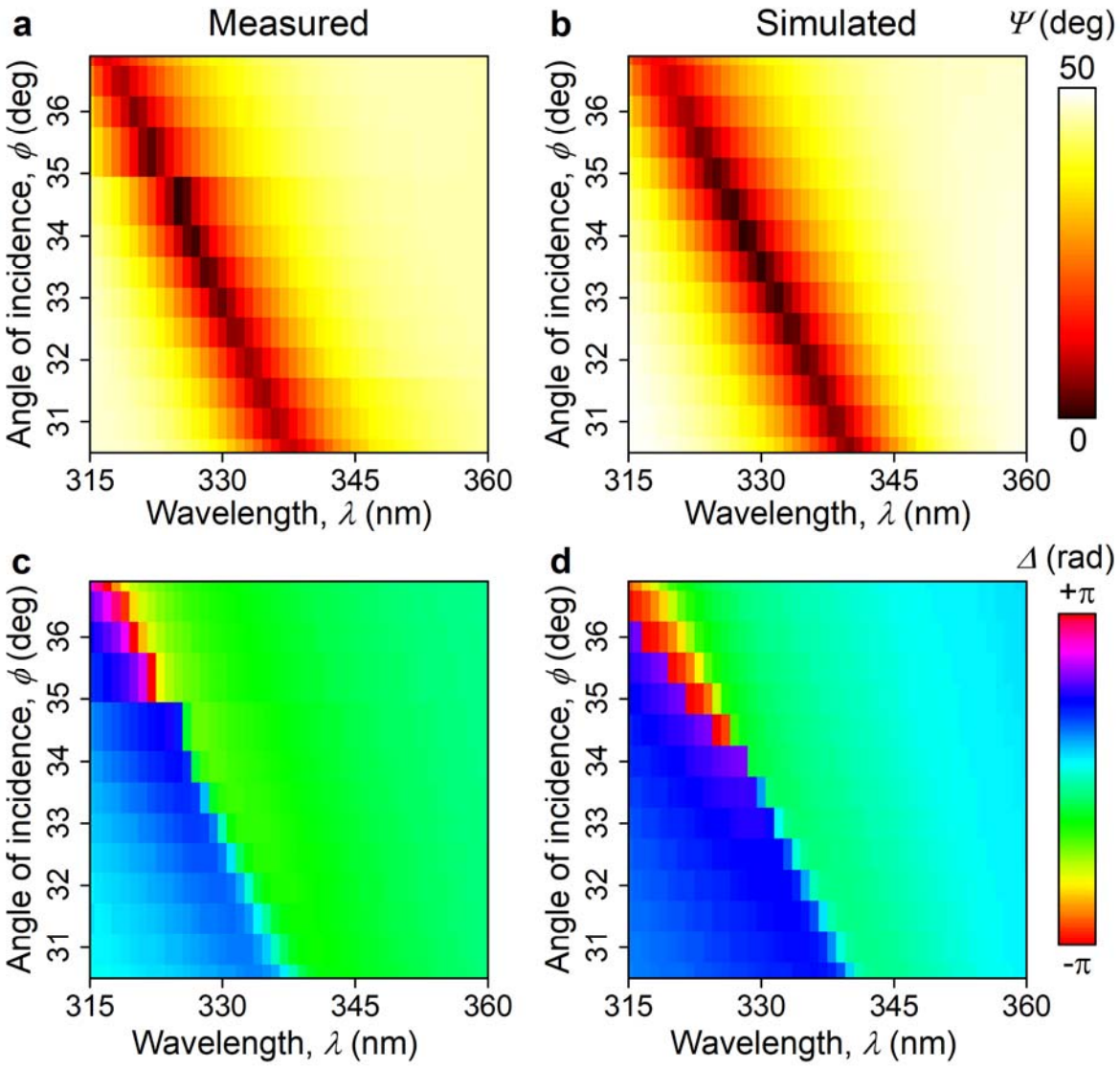

Supplementary Figure 8. Topological point of $PdSe_2$ in water. a-b Experimental and **c-d** simulated ellipsometric parameters Ψ (amplitude) and Δ (phase) for the system water/$PdSe_2$/SiO_2/Si.

Supplementary Note 6: Impossibility of existence of the higher-order topological charges on the r_p and r_s maps

1) Reflection coefficient near the topological point

Without loss of generality, we will start with the expression for the reflection coefficient for p-polarization:

$$r_p = \frac{\frac{\varepsilon_2 q_{1z}}{\varepsilon_1 q_{2z}}\left(\frac{q_{2z}}{\varepsilon_2}\cos k_{2z}\, d - i\frac{q_{3z}}{\varepsilon_3}\sin k_{2z}\, d\right) - \left(1 - 2\alpha\frac{q_{1z}}{\varepsilon_1}\right)\left(\frac{q_{3z}}{\varepsilon_3}\cos k_{2z}\, d - i\frac{q_{2z}}{\varepsilon_2}\sin k_{2z}\, d\right)}{\frac{\varepsilon_2 q_{1z}}{\varepsilon_1 q_{2z}}\left(\frac{q_{2z}}{\varepsilon_2}\cos k_{2z}\, d - i\frac{q_{3z}}{\varepsilon_3}\sin k_{2z}\, d\right) + \left(1 + 2\alpha\frac{q_{1z}}{\varepsilon_1}\right)\left(\frac{q_{3z}}{\varepsilon_3}\cos k_{2z}\, d - i\frac{q_{2z}}{\varepsilon_2}\sin k_{2z}\, d\right)} \quad (9)$$

Near a zero-reflection point ($r_p(\lambda_0,\ \theta_0) = 0$), the reflection coefficient could be represented as

$$r_p = \frac{\partial r_p}{\partial \lambda}\Delta\lambda + \frac{\partial r_p}{\partial \theta}\Delta\theta + \mathcal{O}\left(\sqrt{\frac{\Delta\lambda^2}{\lambda_0^2} + \frac{\Delta\theta^2}{\theta_0^2}}\right) \quad (10)$$

where $\Delta\lambda = \lambda - \lambda_0$, $\Delta\theta = \theta - \theta_0$, and $\frac{\partial r_p}{\partial \lambda}$ and $\frac{\partial r_p}{\partial \theta}$ are calculated in $(\lambda_0,\ \theta_0)$ point. Rewriting $r_p\ as$:

$$\left(\mathrm{Re}\left[\frac{\partial r_p}{\partial \lambda}\right]\Delta\lambda + \mathrm{Re}\left[\frac{\partial r_p}{\partial \theta}\right]\Delta\theta\right) + i\left(\mathrm{Im}\left[\frac{\partial r_p}{\partial \lambda}\right]\Delta\lambda + \mathrm{Im}\left[\frac{\partial r_p}{\partial \theta}\right]\Delta\theta\right) = \Delta x + i\Delta y = \Delta z, \quad (11)$$

we see that the map $(\Delta\lambda, \Delta\theta) \rightarrow (\Delta x, \Delta y)$ is linear, and while it is not degenerate, it transforms a circle into an ellipse with the same center. Therefore, $|C| = 1$.

2) Higher-order charges conditions

To achieve a higher-order singularity, we need that $r_p = \Delta z^{|C|} + \mathcal{O}\left(\Delta z^{|C|+1}\right)$, for some $\Delta z = (A\Delta\lambda + B\Delta\theta) + i(C\Delta\lambda + D\Delta\theta)$. Therefore, at least (necessary but not sufficient) the following conditions must be satisfied:

$$\frac{\partial r_p}{\partial \lambda}(\lambda_0, \theta_0) = 0 \quad (12)$$

$$\frac{\partial r_p}{\partial \theta}(\lambda_0, \theta_0) = 0 \tag{13}$$

Equation $r_p(\lambda_0, \theta_0) = 0$ gives us the condition for the α: $\alpha = f_1(\lambda_0, \theta_0)$, Eqs. (12,13) give the second condition: $\alpha = f_2(\lambda_0, \theta_0)$. As both conditions should be fulfilled simultaneously, $f_1(\lambda_0, \theta_0) = f_2(\lambda_0, \theta_0)$, which means that only several separate points could have non-unitary charge.

Let us now switch to the second representation of the topology and consider the intersection of the material curve with the zero-reflection surface in the point corresponding to $(\lambda_0,\ \theta_0)$. Eq. (13) with the condition $\alpha = f_1(\lambda_0, \theta_0) = f_2(\lambda_0, \theta_0)$ fixes also the derivative of α with respect to the wavelength, which defines the direction of the material curve. Moreover, an infinitesimal change of the material curve's direction leads to the appearance of the linear terms and disappearance of the $|C| > 1$ point. Indeed, one can show that

$$r_p = \left(\mathrm{Re}\left[\frac{\partial r_p}{\partial \lambda}\right]\Delta\lambda + \mathrm{Re}\left[\frac{\partial^2 r_p}{\partial \lambda\, \partial \theta}\right]\Delta\lambda\Delta\theta + \mathrm{Re}\left[\frac{\partial^2 r_p}{\partial \theta^2}\right]\Delta\theta^2\right)$$
$$+ i\left(\mathrm{Im}\left[\frac{\partial r_p}{\partial \lambda}\right]\Delta\lambda + \mathrm{Im}\left[\frac{\partial^2 r_p}{\partial \lambda\, \partial \theta}\right]\Delta\lambda\Delta\theta + \mathrm{Im}\left[\frac{\partial^2 r_p}{\partial \theta^2}\right]\Delta\theta^2\right) \tag{14}$$

corresponds to $|C| < 2$.

For each arrangement of the curve and surface one can find an infinitesimal rotation of the curve which will not lead to the appearance of additional intersections. The rest point will have $|C| < 2$, which means that an initial point also has $|C| < 2$, because of the topological charge conservation.

Supplementary Note 7: Optical system with double topological charge

To theoretically realize zero with double topological charge $C = +2$, we use thin film incorporated in the structure dielectric ($\varepsilon = 5$)/thin film (5 nm)/SiO_2 (300 nm)/Si and with optical constants defined via Lorentz oscillator:

$$\varepsilon = \varepsilon_\infty + \frac{A}{\omega_0^2 - \omega^2 - i\omega\gamma} \tag{15}$$

with $\varepsilon_\infty = 10i$; $A = 10^{-4}$ nm^{-2}; $\lambda_0 = 374.6$ nm, $\omega_0 = 1/\lambda_0$; $\gamma = 0.00324$ nm^{-1}. The resulting topological zero is plotted in Figure 5c of the main text.

Another approach is to use in-plane anisotropy, which greatly helps in the engineering of double topological charge when optical axis of the thin film oriented along with in-plane component of wave vector. It allows independent control of p- and s-polarization response through optical constants of thin film. As an example, the system anisotropic film (5 nm)/SiO_2 (280 nm)/Si yields double topological charge (Figure 5d) with the following Lorentz parameters for anisotropic film: for optical axis parallel to in-plane wave vector $\varepsilon_\infty = 20$; $A = 10^{-4}$ nm^{-2}; $\lambda_0 = 501.55$ nm, $\omega_0 = 1/\lambda_0$; $\gamma = 0.00021$ nm^{-1}; for optical axis perpendicular to in-plane wave vector $\varepsilon_\infty = 1$; $A = 10^{-5}$ nm^{-2}; $\lambda_0 = 420$ nm, $\omega_0 = 1/\lambda_0$; $\gamma = 0.0002$ nm^{-1}.

SUPPLEMENTARY REFERENCES

1. Wang, Y. *et al.* Atomically Thin Noble Metal Dichalcogenides for Phase-Regulated Meta-optics. *Nano Lett.* **20**, 7811–7818 (2020).
2. Kravets, V. G. *et al.* Spectroscopic ellipsometry of graphene and an exciton-shifted van Hove peak in absorption. *Phys. Rev. B* **81**, 1–6 (2010).
3. Ermolaev, G. A. *et al.* Broadband optical properties of monolayer and bulk MoS_2. *npj 2D Mater. Appl.* **4**, 1–6 (2020).
4. Ermolaev, G. A., Yakubovsky, D. I., Stebunov, Y. V., Arsenin, A. V. & Volkov, V. S. Spectral ellipsometry of monolayer transition metal dichalcogenides: Analysis of excitonic peaks in dispersion. *J. Vac. Sci. Technol. B* **38**, 014002 (2020).
5. Tatarkin, D. E. *et al.* Surface-enhanced Raman spectroscopy on hybrid Graphene/Gold substrates near the percolation threshold. *Nanomaterials* **10**, (2020).

6. Shishkin, M. & Kresse, G. Implementation and performance of the frequency-dependent GW method within the PAW framework. *Phys. Rev. B* **74**, 1–13 (2006).

7. Kresse, G. & Furthmüller, J. Efficient iterative schemes for ab initio total-energy calculations using a plane-wave basis set. *Phys. Rev. B* **54**, 11169–11186 (1996).

8. Kresse, G. & Joubert, D. From ultrasoft pseudopotentials to the projector augmented-wave method. *Phys. Rev. B* **59**, 1758–1775 (1999).

9. Blöchl, P. E. Projector augmented-wave method. *Phys. Rev. B* **50**, 17953–17979 (1994).

10. Perdew, J. P., Burke, K. & Ernzerhof, M. Generalized gradient approximation made simple. *Phys. Rev. Lett.* **77**, 3865–3868 (1996).

11. Goldstein, D. H. *Polarized Light*. (CRC Press, 2017).

12. Yu, J. *et al.* Direct Observation of the Linear Dichroism Transition in Two-Dimensional Palladium Diselenide. *Nano Lett.* **20**, 1172–1182 (2020).

13. Lu, L.-S. *et al.* Layer-Dependent and In-Plane Anisotropic Properties of Low-Temperature Synthesized Few-Layer $PdSe_2$ Single Crystals. *ACS Nano* **14**, 4963–4972 (2020).